CHEMISTRY OF MATERIALS
Article

Chem. Mater. **2009,** *21,* 3883–3888 3883
DOI:10.1021/cm900829g

Photonic Properties of Inverse Opals Fabricated from Lanthanide-Doped $LaPO_4$ Nanocrystals

Anke Oertel,*,† Cornelia Lengler,‡ Thomas Walther,‡ and Markus Haase

†*University of Osnabrück, Institute of Chemistry, Barbarastr. 7, 49069 Osnabrück, and* ‡*Technical University of Darmstadt, Institute for Applied Physics, Schlossgartenstr. 7, 64289 Darmstadt*

Received March 25, 2009. Revised Manuscript Received July 8, 2009

A new method for the preparation of rare-earth doped inverse opal materials is reported. Template structures consisting of ordered stacks of PMMA-spheres were infiltrated with colloidal solutions of luminescent $LaPO_4$:Ln (Ln = Tb^{3+}, Eu^{3+}) nanocrystals containing a small amount of prehydrolyzed tetramethoxysilane as binder. After calcination of the PMMA-template, light-emitting photonic materials with inverse opal structure are obtained. Under UV-excitation the materials display the characteristic luminescence line emission of the lanthanide component. We show that by adjusting the diameter of the PMMA-spheres of the template the photonic band structure of the material can be controlled in a way that modifies the lanthanide luminescence.

Introduction

The highly ordered structures of photonic crystals possess a periodically modulated dielectric constant on a scale of the wavelength of light, in which light can propagate only along angle-dependent directions because of the Bragg diffraction conditions[1] similar to electrons in a crystal structure. Since the early works of John[2] and Yablonovitch[3] photonic band materials have become the subject of considerable research activity. Photonic band materials open a new range of possibilities for the generation and propagation of light.[4] For the fabrication of three-dimensional photonic crystals various techniques have been proposed such as holographic lithography,[5] self-assembly,[6,7] angled-etching,[8] micromanipulation,[9] auto cloning,[10,11] and more. A technologically simple way to produce a photonic band material is based on the self-assembly of monodisperse spheres of silica, polystyrene, polymethylmethacrylate, or other building blocks suspended in a suitable liquid. The process leads to colloidal crystals with a three-dimensional periodic structure, for which the opal is a prominent representative.[12,13]

By replacement of the material-constituent of the photonic structure by voids and vice versa, an "inverted structure" is obtained. The associated procedure usually consists in infiltrating the ordered assembly of spheres or other building blocks with a type of solid-forming material or precursor that is able to completely penetrate the void space between the building blocks. Subsequently, the infiltrated material is converted into a solid and then the template is selectively removed by chemical etching or calcination. This leads to a regular network of macropores, which are interconnected, where the former template units (e.g., spheres) had been in direct contact. In many cases the shrinkage associated with the removal of the template reduces the size of the macropores by 10−30% of the initial structure size.[14−16]

If the basic unit of the periodic skeletal structure is on the length scale of optical wavelengths, a complete gap in the photonic band can occur, and consequently, within a certain range of wavelength, the propagation of light in the materials is forbidden for any direction and state of polarization. A complete photonic band gap in fcc inverse opal structures of regular spherical macropores requires a refractive index >2.8,[17,18] which in the visible was not

*Corresponding author phone: +49 541 969 2383; fax +49 541 969 3323, e-mail: anke.oertel@uni-osnabrueck.de.

(1) Bechger, L.; Lodahl, P.; Vos, W. L. *J. Phys. Chem. B* **2005**, *109*, 9980.
(2) John, S. *Phys. Rev. Lett.* **1987**, *58*, 2486–2489.
(3) Yablonovitch, E. *Phys. Rev. Lett.* **1987**, *58*, 2059–2062.
(4) King, J. S.; Gaillot, D. P.; Graugnard, E.; Summers, C. J. *Adv. Mater.* **2006**, *18*, 1063–1067.
(5) Campbell, M.; Sharp, D. N.; Harrison, M. T.; Denning, R. G.; Turberfield, A. J. *Nature* **2000**, *404*, 53–56.
(6) Vlasov, Y. A.; Bo, X.; Sturm, J. C.; Norris, D. J. *Nature* **2001**, *414*, 289–293.
(7) Blanco, A.; Chomski, E.; Grabtchak, S.; Ibisate, M.; John, S.; Leonard, S. W.; Lopez, C.; Meseguer, F.; Miguez, H.; Mondia, J. P.; Ozin, G. A.; Toader, O.; van Driel, H. M. *Nature* **2000**, *405*, 437–440.
(8) Cheng, C. C.; Scherer, A. *J. Vac. Sci. Technol., B* **1995**, *13*(6), 2696–700.
(9) Aoki, K.; Miyazaki, H. T.; Hirayama, H.; Inoshita, K.; Baba, T.; Shinya, N.; Aoyagi, Y. *Appl. Phys. Lett.* **2002**, *81*, 3122–3124.
(10) Kuramochi, E.; Notomi, M.; Kawashima, T.; Takahashi, J.; Takahashi, C.; Tamamura, T.; Kawakami, S. *Opt. Quantum Electron.* **2002**, *34*, 53–61.
(11) Sato, T.; Miura, K.; Ishino, N.; Othera, Y.; Tamamura, T.; Kawakami, S. *Opt. Quantum Electron.* **2002**, *34*, 63–70.
(12) Xia, Y.; Gates, B.; Yin, Y.; Lu, Y. *Adv. Mater.* **2000**, *12*, 693–713.
(13) Waterhouse, G. I. N.; Waterland, M. R. *Polyhedron* **2007**, *26*, 356–368.
(14) Stein, A.; Li, F.; Denny, N. R. *Chem. Mater.* **2008**, *20*, 649–666.
(15) Norris, D. J.; Vlasov, Y. A. *Adv. Mater.* **2001**, *13*, 371–376.
(16) Stein, A.; Schroden, R. C. *Curr. Opin. Solid State Mater. Sci.* **2001**, *5*, 553–564.
(17) Sözüer, H. S.; Haus, J. W.; Inguva, R. *Phys. Rev. B* **1992**, *45*, 13962.
(18) Busch, K.; John, S. *Phys. Rev. E* **1998**, *58*, 3896.

Published on Web 08/04/2009

realized yet. The optical properties of photonic band materials allow manipulating or guiding of light transmission and may therefore be useful for a number of unique technological applications, including optical waveguides with sharp bends, optical integrated circuits, single-mode diode lasers, and low threshold telecommunication lasers.[19] Photonic band materials have also been suggested as suitable materials for pigments, camouflage (stealth) applications, and sensors. Moreover, the relatively large macropore space provides sufficient room to design structural complexity into the material by functionalization of the walls with molecular groups, clusters, polymers, and nanoparticles.[14] The functionalization with luminescing materials is of particular interest, since in this case the photonic band material can affect not only the incident light but also the emitted light. To retain the photonic band properties of the material, however, an uneven distribution of the infiltrated luminescing material must be avoided, since otherwise a broad distribution of effective pore diameters or even clogging of the macropores will be the result. Therefore, only a thin layer of luminescing material can be applied to the inner surfaces of the macropores that, depending on the absorption cross section of the luminescing material, can result in poor absorption of the excitation light. This problem can be avoided if not only the inner surfaces but the whole photonic band material is composed of luminescing material. In this paper, we show that lanthanide doped $LaPO_4$ nanocrystals are well suited for this approach. Because of their small size and high colloidal solubility the nanocrystals are able to completely penetrate the void space of the template structure. The $LaPO_4$ nanocrystals provide a rigid and well-defined crystal environment for the luminescing lanthanide ions, that, as we will show in this paper, is not affected by the preparation of the inverse opal. Moreover, the luminescence of the lanthanide ions consists of narrow emission lines, which are narrower than the width of the stop band of the photonic material.

Experimental Section

Synthesis of Luminescent Nanoparticles. Eu^{3+} or Tb^{3+} doped lanthanide phosphate nanoparticles were prepared in a high boiling coordinating solvent according to a modified procedure. Either $LaCl_3 \cdot 7H_2O$ (9.5 mmol, 99.9%, Treibacher) and $EuCl_3 \cdot 6H_2O$ (0.5 mmol, 99.9%, Treibacher) or $LaCl_3 \cdot 7H_2O$ (8.5 mmol, 99.9%, Treibacher) and $TbCl_3 \cdot 6H_2O$ (1.5 mmol, 99.9%, Treibacher) were dissolved in 10 mL methanol p.a. To the resulting clear solution, diethyl ethylphosphonate (40 mmol, 98%, Fluka) and Diphenyl ether (30 mL, 98%, Merck) were added and subseqently the methanol was removed at 60 °C on a rotary evaporator. Next, the water released from the hydrated salts was removed under vacuum on a Schlenk line at 105 °C. To the resulting clear solution, tributylamine (40 mmol, 98%, Fluka) and a solution of dry phosphoric acid in dihexyl ether (20 mmol, 98%, Merck) were added and the mixture was heated to 200 °C under dry nitrogen. After 16 h, the heating was stopped and the solution was allowed to cool. The precipitate of nanoparticles was separated by centrifugation and dissolved in 300 mL of methanol. The clear colloidal solution was purified by diafiltration (5000 Da filter, Millipore; Diafiltration cell, Millipore; solvent methanol). By removal of the methanol with a rotary evaporator, the nanoparticles may be isolated from the purified colloid as a white powder (typical > 2 g, yield ≃100%).

Preparation of the Solution for Infiltration. Tetramethyl orthosilicate (TMOS, 98%, Merck) was prehydrolyzed at 70 °C by stirring TMOS, methanol, and H_2O in a volume ratio of 1:0.66:0.5 for about 10 min. The final composition of 70% w/w nanoparticles and 30% w/w SiO_2 was adjusted by adding an appropriate amount of the purified colloidal solution containing 10% w/v nanoparticles in methanol.

Synthesis of Inverse Opals. Aqueous suspensions containing 16 to 24% w/v of monodisperse PMMA microspheres in the size range from 285 to 400 nm were prepared by the polymerization of methylmethacrylate in water as given in the literature.[19] After the synthesis, the suspensions were filtered over glass wool and stored at room temperature. The size of the microspheres is mainly determined by the reaction temperature and the amount of monomer employed. Smaller concentrations of methylmethacrylate and higher temperatures, for instance, favor the formation of smaller PMMA spheres.

A densely closed packed layer of PMMA microspheres was obtained by pouring 50 mL of suspension in a clean Petri dish with a diameter of 9 cm and slowly drying the suspension at 50 °C. The opal structure did form by self-assembly of the microspheres during the complete evaporation of the solvent, which took approximately 2 days. To improve their mechanical stability, the structures were subsequently heated at 100 °C for one hour, i.e., 20 °C below the glass transition temperature of PMMA. In the next step, the opal structure was infiltrated three times with a colloidal solution of luminescent nanocrystals and prehydrolyzed TMOS (see above). After the voids of the PMMA sphere assembly were filled with the colloidal mixture, the structure was dried overnight at 50 °C. Thereafter, the PMMA spheres were removed by calcination. To avoid the formation of carbon residues, the calcination procedure was split into two steps. In the first step, the PMMA was depolymerized and the volatile monomer removed by heating the sample at 350 °C under vacuum for several hours. Remaining organic residues were subsequently oxidized in the second step by heating under normal pressure in air using the following temperature profile: heating from room temperature to 300 at 2 °C min^{-1}, heating at 300 °C for 6 h, heating from 300 to 600 °C at 2 °C min^{-1}, keeping that temperature for at least 12 h, and finally allowing to cool to room temperature (mean cooling rate between 600 and 200 °C, approximately 50 °C/h).

Characterization. X-ray diffraction patterns (XRD) of powder samples were recorded with a PANalytical/X'pert Pro system using Cu Kα radiation. Dynamic light scattering (DLS) measurements were performed on a Malvern Zetasizer. Transmission electron microscope (TEM) images were taken with a Jeol JEM 2100 electron microscope operating with a LaB_6 Cathode and an acceleration voltage of 200 kV. Reflection spectra and Bragg reflexes of inverse opal specimen in Figure 4 were measured with a Cary 6000i UV−vis-NIR absorption spectrometer equipped with a Harrick FiberMate fiber adapter and a Y-glasfiber QBIF600-UV/BX. The reflection spectra were recorded by adjusting the end of the Y-glasfiber approximately 2 mm above the surface of the sample perpendicular to the [111] plane of the reciprocal lattice of the fcc pseudo−crystal and measuring the light intensity reflected from an area of about

(19) Schroden, R. C.; Al-Daous, M.; Blanford, C. F.; Stein, A. *Chem. Mater.* **2002**, *14*, 3305–3315.

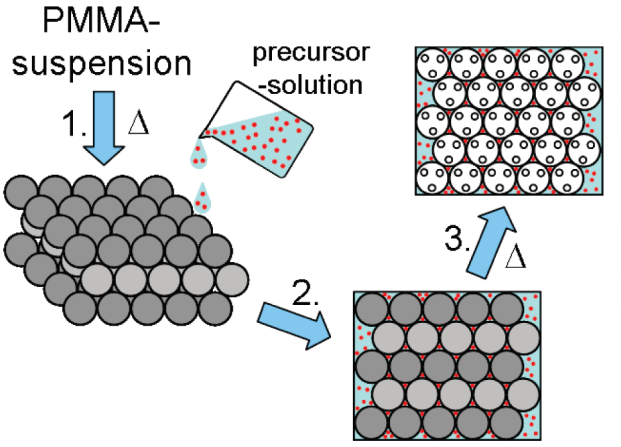

Figure 1. Illustration of the preparation method: A regular stack of PMMA spheres obtained by self-assembly is infiltrated with a colloidal precursor-solution containing a high concentration of doped nanocrystals and prehydrolyzed tetramethoxysilane. After it was dried, the inverse opal structure is obtained by calcination of the PMMA template.

1 mm^2. The intensity values thereby obtained were divided by the corresponding values of a reflectance standard (Spectralon) measured separately under identical conditions. SEM images were taken on a DSM 962 scanning electron microscope (Zeiss). Luminescence measurements of ground powders and of colloidal solution were measured with a Fluorolog 3 fluorescence spectrometer (Jobin Yvon).

Microscopy work was done by fixing the sample on an inverse microscope (Nikon TE 300). UV-light of a high pressure mercury lamp excited the rare earth ions and emission light was collected with an objective (Nikon Plan Fluor 4×/0.13), and detected using the InstaSpecIV CCD-Chip (1024 × 256 Pixel, working temperature −25 °C) of an imaging spectrometer (Oriel MS257). Stop bands in Figure 7 were measured by illuminating the samples with light of a halogen lamp (Mikropack DH-200) and detecting the reflected light with the spectrometer.

Results and Discussion

In this paper, we describe a novel method for the preparation of inverse opals, which is based on the infiltration of a PMMA template structure with a colloidal solution consisting of luminescing rare earth doped lanthanum phosphate nanocrystals and prehydrolyzed tetramethoxysilane in methanol. An illustration of the infiltration procedure is given in figure 1. The resulting inverse opal structure is composed of 70% w/w of nanocrystals and 30% w/w of silicon dioxide, working as a binder for the nanocrystals.

To improve the infiltration efficiency and the structure quality, we replaced the stabilizing agents employed in our earlier nanoparticle synthesis procedure[20−22] by diethyl ethylphosphonate and tributylamine, that is, by surface ligands with shorter alkyl chain length. The shorter alkyl chains of these ligands improve the colloidal solubility[23] of the particles in polar solvents like methanol and reduce the amount of organic material that has to be removed by calcinations. Colloidal solutions containing more than 10% w/v of nanocrystals in methanol were used for infiltration (Figure 2). This modification of the synthesis, however, only weakly affects the size of the resulting nanoparticles. Figure 2 shows TEM images of the particles and the size distribution in solution as determined by dynamic light scattering. Both methods indicate a similar particle size distribution ranging from approximately 5 to 9 nm (FWHM).

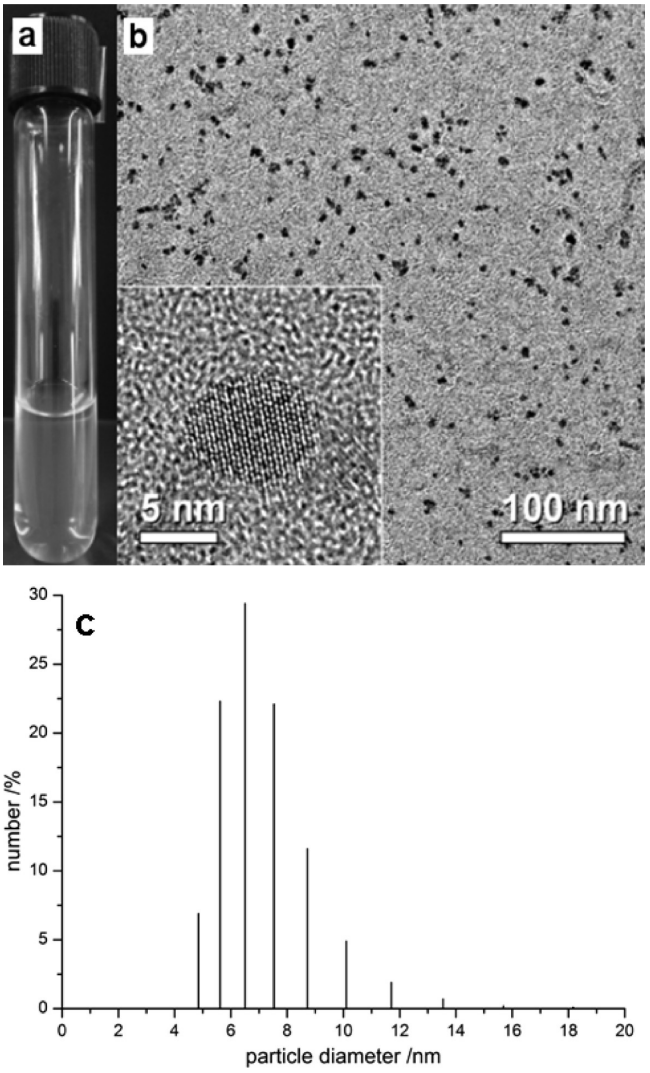

Figure 2. Image of a highly concentrated colloid of redispersed $LaPO_4$:Tb nanoparticles (a), TEM images of $LaPO_4$:Tb nanocrystals (b), and distribution of the hydrodynamic diameters of $LaPO_4$:Tb nanoparticles in methanol as determined by dynamic light scattering (c).

After the voids of the PMMA sphere assembly were filled with the colloidal mixture of nanocrystals and SiO_2 precursor, the structure was dried overnight at 50 °C and afterward the PMMA spheres were removed by calcination (see Experimental Section for details). SEM images of a sample prepared with 330 nm PMMA template

(20) Lehmann, O.; Meyssamy, H.; Kömpe, K.; Schnablegger, H.; Haase, M. *J. Phys. Chem. B* **2003**, *107*, 7449–7453.
(21) Riwotzki, K.; Meyssamy, H.; Schnablegger, H.; Kornowski, A.; Haase, M. *Angew. Chem. Int. Ed.* **2001**, *40*, 573–576.
(22) Kömpe, K.; Borchert, H.; Storz, J.; Lobo, A.; Adam, S.; Möller, T.; Haase, M. *Angew. Chem. Int. Ed.* **2003**, *42*, 5513–5516.
(23) Hickmann, K.; Kömpe, K.; Hepp, A.; Haase, M. *Small* **2008**, *4*, 2136–2139.

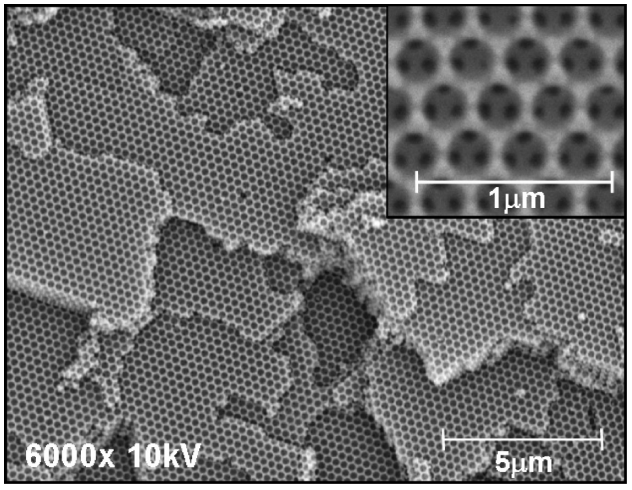

Figure 3. SEM image of the inverse opal structure. The material consists of 70% w/w $LaPO_4$:Tb and 30% w/w SiO_2. PMMA spheres with a diameter of 330 nm were used in the synthesis.

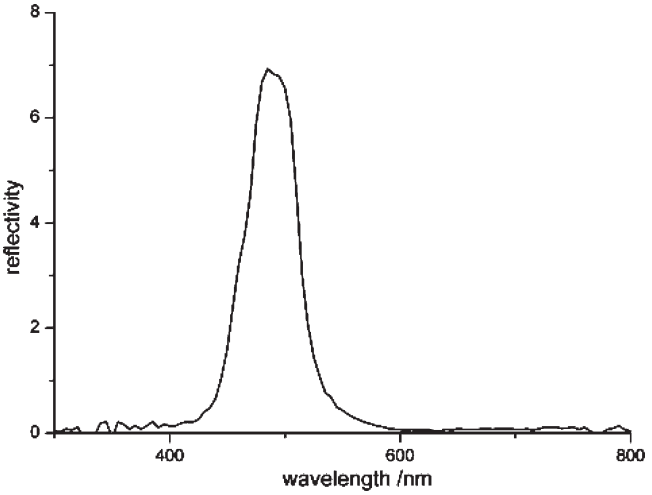

Figure 4. Reflection spectrum of an inverse opal displaying the Bragg reflex. The macropores in the inverse opal had a mean diameter of 260 nm.

spheres are shown in Figure 3 as an example. The images show a highly ordered inverse opal structure, resembling the densely close packed arrangement of the former PMMA spheres. After the template was removed, the resulting macropores exhibit a mean diameter of 280 nm, indicating that shrinkage has occurred during calcination.

It is well-known that inverse opal structures display a photonic stop band in [111] direction.[13] In fact, the reflection spectra of coarse powders as well as of flat specimen of the inverse opal materials display a strong Bragg reflex because of the stop band of the photonic bandgap.

Figure 4 displays the stop band of one of our inverse opal materials prepared with 315 nm PMMA template spheres resulting in macropores with an average diameter of 260 nm. If the stop band (Bragg reflex) is measured at

(24) Schroden, R. C.; Al-Daous, M.; Stein, A. *Chem. Mater.* **2001**, *13*, 2945–2950.

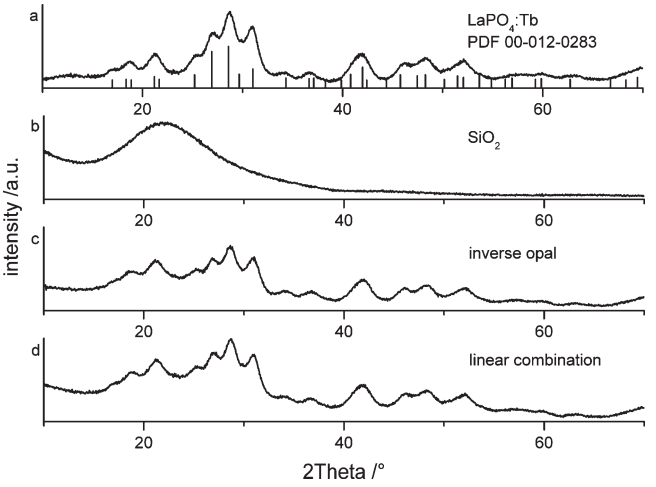

Figure 5. XRD patterns of (a) $LaPO_4$:Tb nanoparticles (line positions of the $LaPO_4$ monazite structure according to PDF 00-012-0283), (b) a SiO_2 inverse opal (after grinding), and (c) an inverse opal of $LaPO_4$:Tb/SiO_2 (after grinding). (d) A linear combination $I_d = 0.8I_a + 0.2I_b$ of the diffractograms a and b reproduces quite well the diffratogram c of the inverse opal.

normal incidence, its spectral position λ at 490 nm is connected with the distance d of the lattice planes of the photonic crystals by the equation[24]

$$\lambda = d\frac{2}{m}\sum \phi_i n_i$$

where $m = 1$ is the order of the Bragg reflex. The sum expression represents the effective refractive index of the inverse opal, which is given by the volume fractions $\phi_{LaPO_4} = 0.13$, $\phi_{SiO_2} = 0.13$, and $\phi_{air} = 0.74$ of $LaPO_4$, SiO_2, and air, respectively, and the corresponding refractive indices $n_{LaPO_4} = 1.8$, $n_{SiO_2} = 1.5$, and $n_{air} = 1.0$. For a densely close-packed layer of spheres (or spherical voids) with diameter D the distance d of the lattice planes in the direction of stacking is given by $d = D\cdot(2/3)^{1/2}$. For a cubic close-packed layer this direction corresponds to the [111] direction of the fcc unit cell. When the expressions for d and the values of the ϕ_i and n_i are inserted into the equation above, the spectral position λ of the stop band is given by

$$\lambda = D\cdot 1.9$$

Thus, the size of the PMMA microspheres determines the size of the macropores as well as the spectral position of the Bragg reflex.[14]

Figure 5 displays the XRD data of as-prepared nanoparticles and inverse opal materials after grinding. The peak positions and intensities in the XRD data of the as-prepared $LaPO_4$:Tb nanoparticles are in accord with the monoclinic monazite phase of the bulk material (Figure 5a). By use of the Scherrer formula, a mean particle size of approximately 5 nm is estimated from the width of the peaks. A similar peak width is observed in the XRD data of the ground inverse opal (Figure 5c), indicating that the calcination steps do not significantly increase the size of the $LaPO_4$:Tb nanoparticles. The

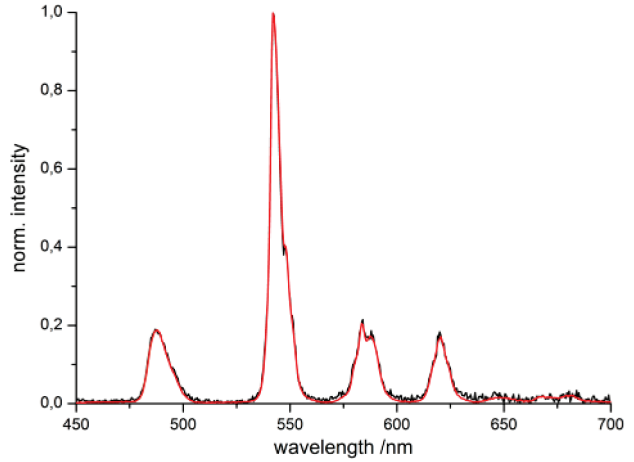

Figure 6. Emission spectrum of $LaPO_4$:Tb nanoparticles (red line) and of an inverse opal (containing $LaPO_4$:Tb nanoparticles, 70% w/w) after grinding (black line).

different background in both diffractograms is caused by the SiO_2 content of the inverse opal material, as shown by the diffractograms in Figure 5b and d. Figure 5b displays the XRD data of a ground inverse opal prepared without $LaPO_4$:Tb nanoparticles, that is, with a colloidal solution containing prehydrolyzed TMOS only. The XRD data indicate that the resulting SiO_2 material is amorphous. Figure 5d shows that the XRD data given in Figure 5c for the inverse opal ($LaPO_4$:Tb and SiO_2) is well reproduced by a linear combination of the diffractogram of the SiO_2 material (Figure 5c) and the diffractogram of the as-prepared particles (Figure 5a).

The crystal lattice of $LaPO_4$ provides a rigid environment for the lanthanide dopant and determines its emission properties. In the case of nanoparticles, however, a significant number of dopant ions are located at the particle surface where the crystal field is different compared with lattice sites in the center of the nanoparticle or the bulk material. For the case of Eu^{3+}-doped $LaPO_4$ nanocrystals, it has, in fact, been shown that the presence of Eu^{3+} ions in surface sites leads to an inhomogeneous broadening of the emission lines in the luminescence spectrum of the particles.[25] To exclude that the quantum yield of dopant ions in surface sites and, hence, their contribution to the overall emission spectrum of the particles is affected by the calcination steps, we compare in Figure 6 the emission of the ground inverse opal with the emission of the nanocrystals directly after the particle synthesis. The Figure proves that the emission bands of the f−f-transitions of the Tb^{3+} dopant are not affected by calcination. At the same time we can infer that the grinding process only destroys the opaline structure but does not affect the structure on the scale that is relevant for defining the lanthanide environment.

When the structure of the inverse opal is intact and the spectral position of one of the emission lines overlaps with the stop band of the structure the observed emission

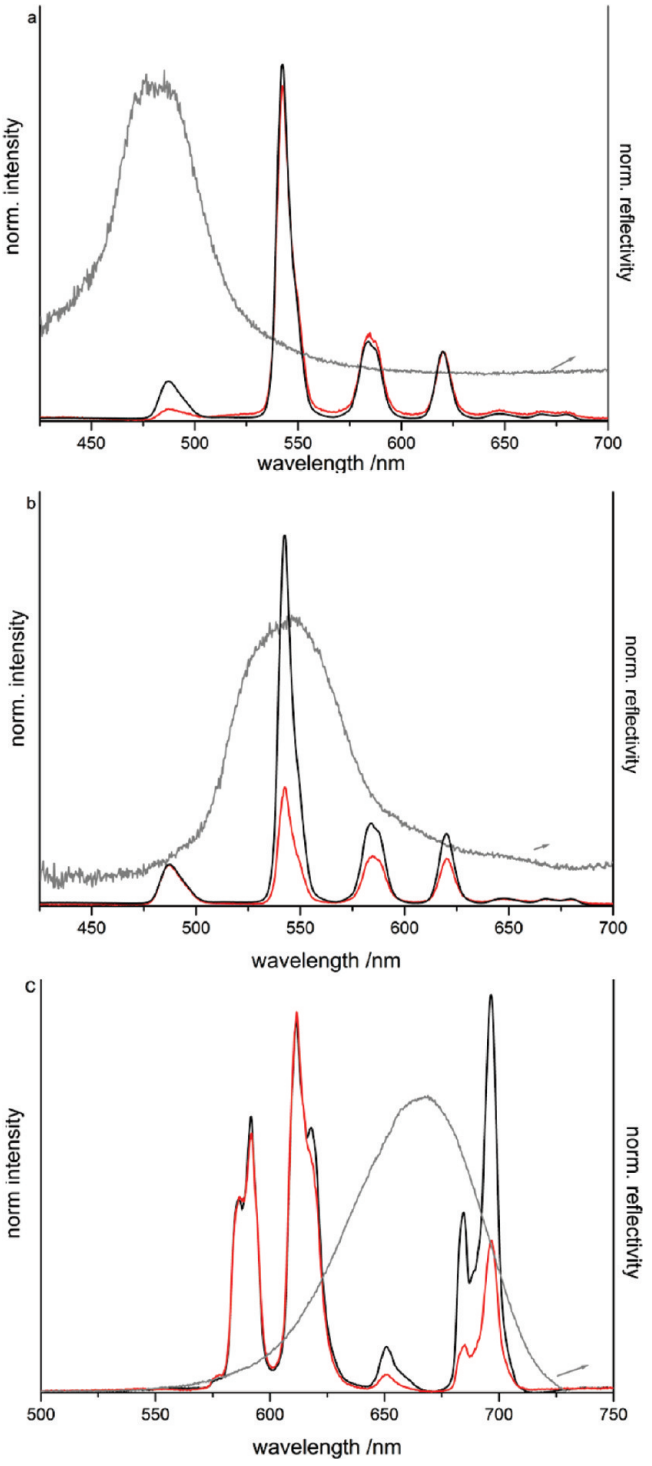

Figure 7. (a) Tb^{3+} emission spectrum of inverse opals for the case of overlap between the stopband and the emission peaks (red line, stopband from 460 to 505 nm) and for the ground sample (black line). (b) The same as in (a) but with overlapping stopband from 515 to 570 nm. (c) Eu^{3+} emission spectrum for the case of overlap between the stopband and the emission peaks (red line, stopband from 630−695 nm) and for the ground sample (black line).

intensity is significantly reduced. To characterize this interaction of the luminescence emission with the photonic [111] band of the inverse opal, a flat specimen (ca. 3 mm × 3 mm in size) was mounted on the sample holder of an inverse microscope with the [111] surface pointing toward the microscope objective. An objective (4×) with

(25) Lehmann, O.; Kömpe, K.; Haase, M. *J. Am. Chem. Soc.* **2004**, *126*, 14935.

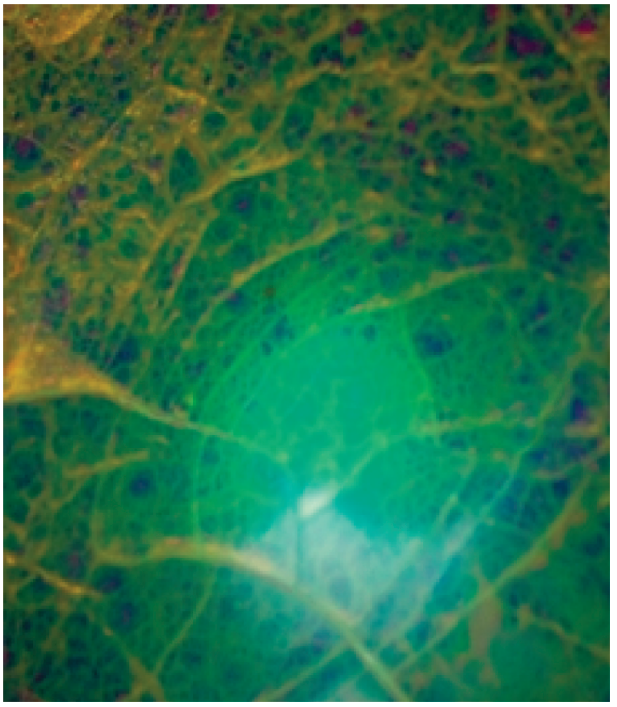

Figure 8. Microscope image of an inverse opal under UV-light. The stopband of the inverse opal ranges from approximately 520 to 580 nm as given in Figure 7b (magnification 4×; inverse fluorescence microscope).

a small numerical aperture of only 13° collected the luminescence emitted in [111] direction. Through the same objective, the sample was either illuminated with UV-light to excite its luminescence or with white light to measure its reflection spectrum.

In Figure 7, the luminescence and reflection spectra of Tb^{3+}- and Eu^{3+}-doped inverse opals are shown. In each case, we juxtapose the emission spectra of a sample with intact and removed (by grinding) photonic structure (i.e., analogous to Figure 6). Each spectrum pair was normalized to an emission peak that lies as far outside the photonic influence of the stop band as possible.

In all cases, the emission intensity is significantly reduced in the spectral region of the stopband.[26] The terbium-doped samples given in Figure 7a and Figure 7b show the typical emission bands of the Tb^{3+}ion, which correspond to the $^5D_4 \rightarrow {}^7F_n$ ($n = 3-6$) transitions of the ion. The emission peaks are located at 487 ($^5D_4 \rightarrow {}^7F_6$), 542 ($^5D_4 \rightarrow {}^7F_5$), 583 ($^5D_4 \rightarrow {}^7F_4$), and 620 nm ($^5D_4 \rightarrow {}^7F_3$). In Figure 7a the Tb transition at 487 nm is affected only because the stopband of the material ranges from approximately 460 and 505 nm (FWHM). When the peak at 620 nm is used to normalize the intensity of the two emission spectra of Figure 7a, the intensity of the peak at 487 nm is reduced by a factor of 3.2 whereas the peak intensities at 542 and 583 nm are not significantly affected (factors of 1.1 and 0.9, respectively). Figure 7b also shows a Tb^{3+}-doped sample, but in this case larger PMMA spheres with a diameter of 375 nm have been used in the synthesis resulting in a stopband between 515 and 570 nm. As a consequence, now the Tb transition at 542 nm is reduced in intensity. Normalization at 487 nm yields factors of 3.2, 1.7, and 1.6 for the intensity reduction of the peaks at 542, 583, and 620 nm, respectively. Finally, Figure 7c displays a similar effect for a Eu^{3+}-doped sample displaying a stopband located between 630 and 695 nm. The emission of this sample is characterized by the $^5D_0 \rightarrow {}^7F_J$ ($J = 1-4$) transitions of the Eu^{3+} ion located in the spectrum at 590 ($^5D_0 \rightarrow {}^7F_1$), 611 ($^5D_0 \rightarrow {}^7F_2$), 651 ($^5D_0 \rightarrow {}^7F_3$), and 696 nm ($^5D_0 \rightarrow {}^7F_4$). Normalization of the emission intensity at 590 nm shows that the transitions at 651 and 696 nm are reduced in intensity by factors of 2.5 and 2.7, respectively.

Whereas the spectra in Figure 7 clearly reveal the interaction of the photonic structure of the material with the emission properties of the embedded luminescing centers none of the emission peaks appears to be completely quenched as theory predicts for the emission mode along the ⟨111⟩-direction. One reason for this is related to the observational method: The microscope objective collects the emission within a cone of 13° emission and thus also picks up the emission of modes outside the "L-stopband", experimentally that corresponds to picking up a large set of plane wave modes in addition to the one that propagates exactly perpendicular to the [111] surface of the samples. For the same reason no attempt was made to measure a possible enhancement of the emission in the fringe of the stopband.[27] The other reason is that the material is not single domain, and at the domain boundaries, cracks open escape paths for luminescence light generated inside the structure through scattering.

In fact, Figure 8 shows that light emitted at these cracks superposes with a different color than the light emitted from the [111] surface. The contribution of the crack-emission to the luminescence spectrum is probably the main reason why still some fluorescence is detected inside the stop band.

Acknowledgment. We thank Henning Eickmeier and Dr. Karsten Kömpe for the TEM investigations, Marianne Gather for measuring the X-ray powder diffractogram. Furthermore we thank A. Weick from the TU-Darmstadt for the SEM images and Dr. Tim Vosgröne at Merck AG for providing assistance with the preparation of microsphere samples. Furthermore we thank Dr. Franco Laeri for fruitful discussions and for careful proof reading of the manuscript. Finally, funding of the project (HELIOS grant number 13N8635) by the BMBF is greatly acknowledged.

(26) Yang, Z.; Zhou, J.; Huang, X.; Yang, G.; Xie, Q.; Sun, L.; Li, B.; Li, L. *Chem. Phys. Lett.* **2008**, *455*, 55–58.

(27) Bovero, E; Van Veggel, F. C. J. M. *J. Am. Chem. Soc.* **2008**, *130*, 15374–15380.